Article

Effects of Microstructural Arrangement on the Mechanical Behavior of 3D Printed Polyamide

Lotfi Hedjazi [1], Sofiane Belhabib [2], Nicolas Stephant [3], Sylvie Durand [4] and Sofiane Guessasma [4,*]

[1] ESTP Campus de Troyes, 1 Rue Fernand Sastre, 10430 Rosières-prés-Troyes, France; lhedjazi@estp.fr
[2] GEPEA, Université de Nantes, Oniris, CNRS, UMR 6144, F-44000 Nantes, France; sofiane.belhabib@univ-nantes.fr
[3] Institut des Matériaux de Nantes Jean Rouxel (IMN), Nantes Université, CNRS, F-44000 Nantes, France; nicolas.stephant@univ-nantes.fr
[4] INRAE, Research Unit BIA UR1268, Rue de la Géraudière, F-44316 Nantes, France; sylvie.durand@inrae.fr
[*] Correspondence: sofiane.guessasma@inrae.fr

Abstract: This study aims to relate the microstructural arrangement, in particular the symmetry materialized by filament sequencing in the fused filament fabrication process, to the mechanical behavior of printed polyamide. Dog-bone structures were printed using various printing temperatures ranging from 250 °C to 280 °C, which were combined with part orientation including vertical, horizontal, and lateral configurations and raster angles (0°, 15°, 30°, and 45°) that represent the in-plane and out-of-plane symmetrical arrangement of the filament. Mechanical testing was conducted on both as-received filaments and printed structures to derive the effects of filament arrangement symmetry and process-generated defects on mechanical loss. In addition, a microstructural analysis using scanning electron microscopy was used to share more light on the filament arrangements and their consequence on the deformation mechanisms with respect to the printing conditions. The results showed that the 3D printed polyamide-based materials exhibited remarkable tensile performance with strain stiffening behavior and large elongation at break due to their particular filament layout. Among the considered printing conditions, the part orientation was found to have the largest influence on the tensile behavior, which modulates the behavior from complete restoration of the filament performance to mechanical loss.

Keywords: fused filament fabrication; polyamide; symmetrical filament arrangement; 3D printing; scanning electron microscopy; tensile properties

1. Introduction

Additive manufacturing (AM) is the process of joining material layer-by-layer, which allows for significant freedom in material arrangement symmetry while decreasing the dependence on manufacturing tools [1]. According to ISO/ASTM 52900:2021 [2], AM is an additive technology material extrusion that can be defined as the process of joining materials to obtain parts from 3D digital model, usually layer upon layer, as opposed to subtractive manufacturing and formative manufacturing methodologies. This process is further subdivided into a collection of processes including fused deposition modelling or fused filament fabrication or FFF [3]. FFF is a widely used AM technology that operates by layering and melting thermoplastic filament materials to create three-dimensional objects [4]. In this process, a computer-controlled extrusion nozzle deposits the molten material layer-by-layer onto a build platform, with each layer fusing to the previous one as it cools and solidifies [5]. FFF is favored for its versatility, accessibility, and affordability, making it a popular choice for desktop 3D printers, especially for processing polymeric materials such as PLA (polylactic acid) and ABS (acrylonitrile butadiene styrene) [6–8]. It is used in a wide range of applications, from rapid prototyping [9] and custom part production [10] to active materials [11], enabling complex designs to be processed with

precision and efficiency [12]. The simplicity and adaptability of FFF have contributed to its prominence in the field of additive manufacturing, allowing a large spectrum of materials to be considered as feedstock materials from monophasic materials such as copolyester [13], polyurethane [14], and acrylonitrile styrene acrylate (ASA) [15] to composite materials such as PLA-flax [16], PLA-hemp [17], and PLA-wood [18].

FFF has become a popular way to process thermoplastics by exploiting their ability to shift from glassy to rubbery states [19]. The laydown and rapid solidification process defines the thermal cycling throughout the part building process [20]. Such technology offers wider possibilities for structuring materials at the microstructural level, where symmetry and asymmetry can be controlled to produce phenomena such as anisotropy. For instance, Uralde et al. [21] tackled the application of symmetry for metal additive manufacturing. The authors pointed out the role of symmetry at the microstructural level to induce anisotropic behavior. Other more focused works such as that by Jagadeesh et al. [22] have discussed the symmetrical gradients of porosities induced by additive manufacturing.

However, the fused filament process generates two dimensional discontinuities in the space, which consequently creates a dependence of the properties of the printed parts on the direction of testing [23]. Ahn et al. [23] discussed the sensitivity of the mechanical behavior of printed ABS material to the relative orientation of the part with respect to the loading direction. The authors concluded that the anisotropic behavior is mainly explained by a lower cohesion in the building direction in comparison to the other in-plane directions. Geometrical effects such as the symmetry in the filament arrangement are among the factors that prevail for controlling the mechanical behavior of printed parts [24]. In a more recent work by the authors [24], the significance of the anisotropic behavior has been proven for a composite material for which both the part orientation and printing angles were found to be important factors for inducing microstructural asymmetric/symmetric architectures. Because of the influence of the material discontinuities, especially the process-generated porosities [25], in comparison to injection molding, a strong trend for considering high-value feed stock materials has been considered for improving the performance of 3D printed materials using FFF. Fayazbakhsh et al. [25] studied the effects of defects on the tensile properties of 3D printed parts. The authors showed that directional properties are affected by defects in the transverse and longitudinal directions, which, depending on their intensity, may induce significant a reduction in the performance. Polyamide and its composites are one of these technical filaments that have received much attention [26]. Sgrulletti et al. studied the correlation between the printing conditions on polyamide 6 mechanical performance using a monitoring technique. The study demonstrated that the bed temperature has a great influence on the mechanical properties of the printed polyamide 6. Arigbabowo et al. [27] studied the FFF printability of a polyamide 6 nanographene composite. The study described a negative effect of nanographene platelet reinforcement on the elongation at break, toughness, and improvement of stiffness and tensile strength. Belei et al. [28] considered FFF of short carbon fiber-reinforced polyamide. The authors showed that the reinforcing effect resulted in limited plasticity. They also observed a strong correlation between the mechanical performance and the printing conditions, including layer height and printing bed temperature.

In the present study, we focused on several printing parameters such as the printing temperature, the part orientation, and the filament arrangement of polyamide-based material on the tensile performance. Among the considered printing conditions, both the part orientation and the printing angle affected the filament arrangement symmetry with respect to the loading direction. For instance, an in-plane arrangement with a printing angle of $0°$ generated layups of $-45°/+45°$. These in-plane layups were shifted to other configurations such as $-30°/+60°$ when the printing angle was modified to $15°$. In addition, the out-of-plane arrangement also created a different material structuring in the building direction, allowing anisotropy of the mechanical behavior to develop. In this study, the part orientation and printing angles were considered as the main parameters related to the

symmetry of filament arrangement in the three-dimensional space. These were expected to significantly influence the deformation mechanisms and the overall tensile behavior.

2. Experimental Layout

2.1. Materials

The feedstock material considered in this study is a commercial polyamide-based (PLDA) filament with a 1.75 mm diameter and a density of 1.12 g/cm^3 from Polymaker company (Shanghai, China) under the tradename polyamide CoPA. The filament was a blend composed of PA6 and PA66. The recommended printing settings were as follows: printing temperature between 250 °C and 270 °C, printing speed within the range 30–50 mm/s, and bed temperature between 25 °C and 50 °C. The main physical properties of the feedstock material are given in Table 1.

Table 1. Main physical parameters of the nylon/polyamide-based filament.

Mechanical Properties		Thermal Properties	
Young's modulus	2223 ± 199 MPa	Glass transition temperature	67 °C
Tensile strength	66.2 ± 0.9 MPa	Vicat softening temperature	180 °C
Bending strength	97.0 ± 1.1 MPa	Melting temperature	190 °C
Charpy impact strength	9.6 ± 1.4 kJ/m^2		

2.2. Manufacturing Process

Dog-bone geometries were printed with the typical dimensions $80 \times 20 \times 4$ mm^3, where the gauge width and length were 10 mm and 20 mm, respectively.

The printing process was conducted using Raise3D Pro2 Plus. The reference printing parameters are shown in Table 2. Three main parameters were varied: the printing temperature Tp (250 °C, 260 °C, 270 °C, 280 °C), the part orientation φ (vertical, horizontal, lateral), and the printing angle θ (0°, 15°, 30°, 45°). The symmetry in the filament arrangement was tuned in the in-plane direction using the printing angle, while the part orientation influenced the material structuring in the building direction. Figure 1 shows the printing configuration for all the considered orientations. The filament arrangement corresponded to filament symmetrical layups of ($-45°/+45°$, $-30°/+60°$, $-15°/+75°$, $0°/90°$, respectively.

Table 2. Process parameters used to obtain 3D printed polyamide.

Parameter	Value	Parameter	Value
Layer height	0.3 mm	Printing speed	50 mm/s
Infill rate	100%	Support density	10%
Nozzle diameter	0.4 mm	Frame width	0.6 mm
Bed temperature	60 °C	Support strategy	everywhere
Printing angle	0–90°	Printing temperature	250–280 °C

For both vertical and lateral orientations, the presence of support material was required. This was performed using the same material, with infill rates as large as 30%. The printing duration for all the samples was approximately 15 min.
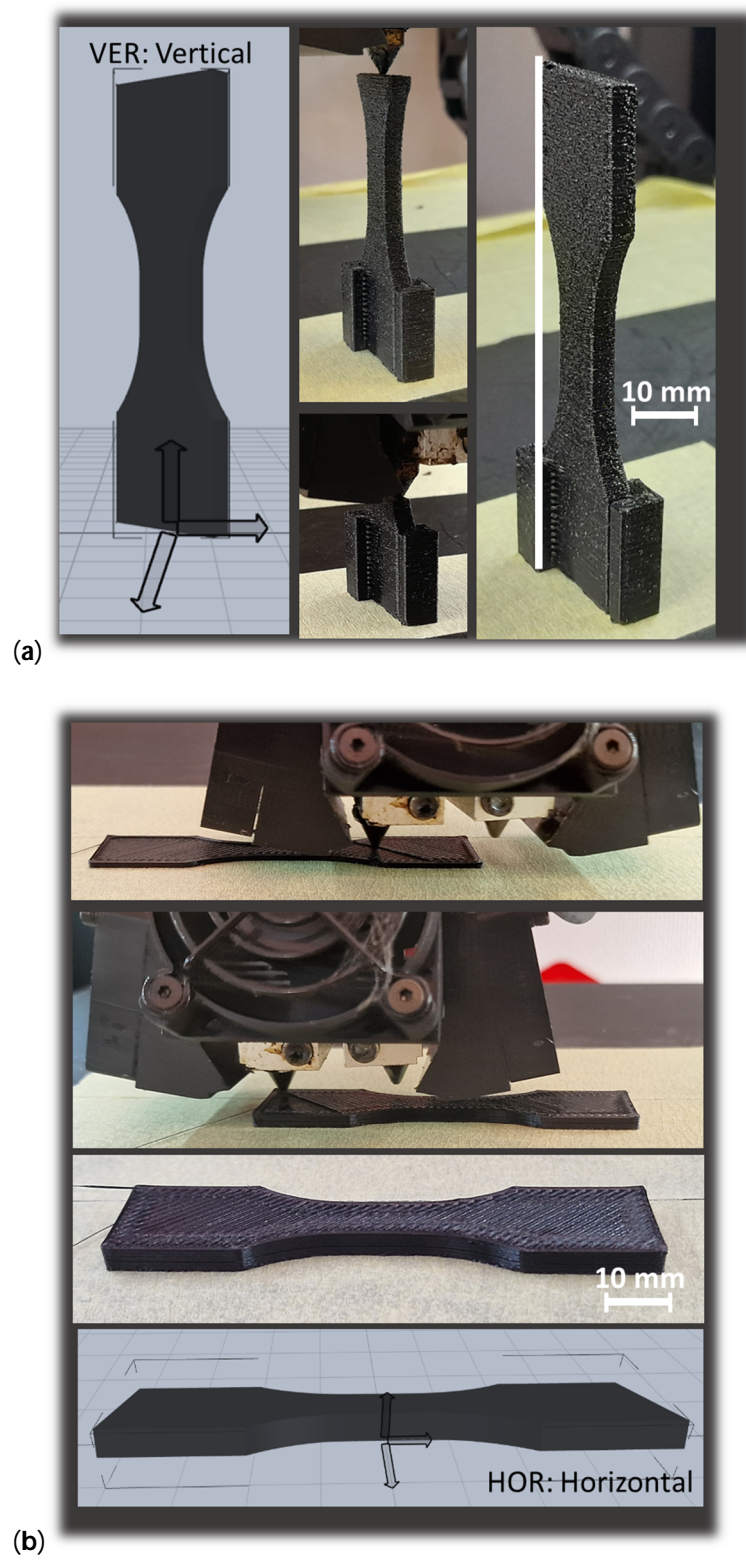
(**a**)

(**b**)

Figure 1. *Cont.*

Figure 1. Ongoing 3D printing process of PLDA and three main orientations considered in this study: (**a**) vertical-VER, (**b**) horizontal–HOR, and (**c**) lateral-LAT.

2.3. Testing Methods

The compositions of the as-received filaments were analyzed using mid-infrared spectroscopy. A Thermo Nicolet IS50 spectrometer (Thermo Scientific, Courtaboeuf, France) serves this purpose. The spectra were acquired according to the reflexion mode between 4000 and 400 cm^{-1} at 16 cm^{-1}, and the Smart iTX-ATR diamond accessory was used. The infrared spectra are the combination of 200 scans, which were processed using OMNIC 9.2.41 software. All spectra in the 4600–4000 cm^{-1} region were processed by finding the baseline, and they were normalized according to the unit vector. The average spectra were computed using 5 replicates. The OPUS version 7.5 software (Bruker Optics, Champs-sur-Marne, France) was used for all the processing steps. The spectra were identified based on a comparison with as-built spectra from the OPUS library. The main components of the PLDA feedstock material were identified according to this technique.

Uniaxial tensile experiments were conducted using the ProLine 10 kN universal machine from Zwick Roell Group (Ulm, Germany) under a displacement rate of 10 mm/min up to the rupture limit of the specimen (Figure 2). Both wire and printed structures were tested. Four replicates per condition were used to ensure a reliable measurement. The deformed specimens were monitored using a high-speed camera (Phantom V7.3, Photonline, Marly Le Roi, 78-France) under various frame sizes and rates.
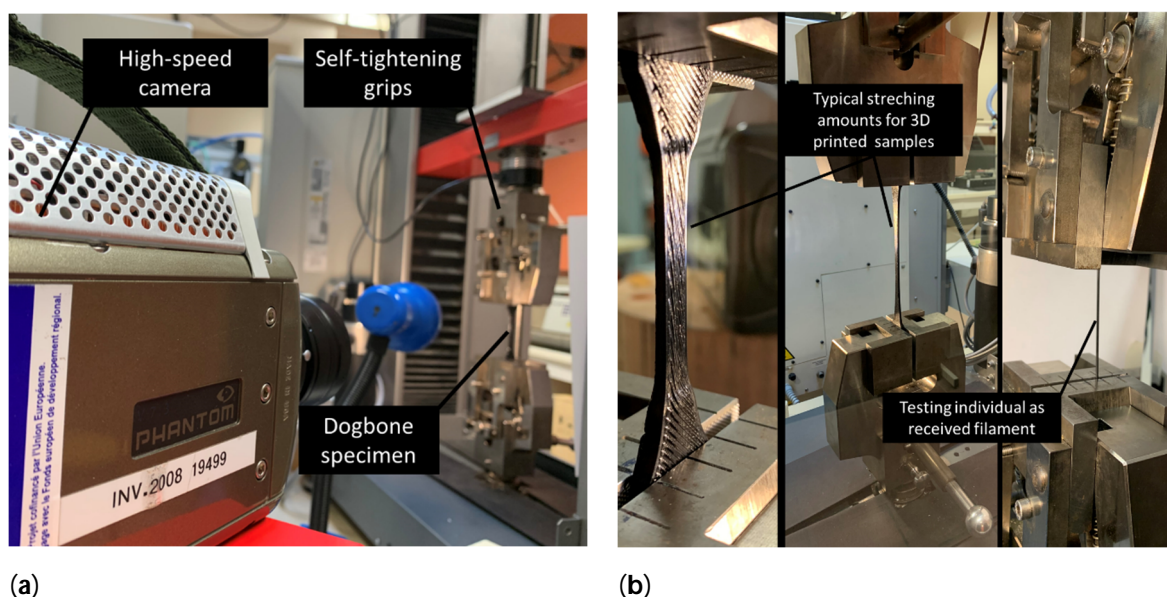
Figure 2. (**a**) Sample testing configuration of PLDA printed material, (**b**) overview of the stretching amounts for both as-received and printed PLDA materials.

Figure 2 shows the typical testing configurations for various printing conditions. The force–displacement data were converted to into engineering stress and strain curves, allowing for engineering quantities such as Young's modulus, E_Y), yield stress σ_Y, tensile strength σ_C, ultimate stress σ_M, and elongation at break E_C to be extracted. All these parameters were related to the printing conditions (θ, ϕ, Tp).

The microstructures of the printed structure as well as their fracture patterns were characterized using scanning electron microscopy (SEM) to check the extent of material symmetry modification. Prior to the observation, all the samples were coated with a carbon layer approximately 50 nm thick using a Balzers CED30 evaporator (Balzers, Liechtenstein). The images were taken with a JEOL JSM 5800 LV microscope operating at 10 KV (Akishima, Japan). The secondary electron detector was used for magnifications ranging from 23$\times$ to 170$\times$ and pixel sizes from 1.56 to 11 μm. One sample per condition was used for the SEM acquisitions.

3. Results and Discussion

3.1. Intrinsic Properties of As-Received PLDA Filament

Figure 3 shows a typical FTIR-ATR spectrum of the studied PLDA filament. The spectrum was compared to a typical polyamide material. The main component present in the filament was polyamide 6 compound. The infrared assignment characteristic of this compound was the N-H amide stretching in the 3100–3500 cm^{-1} domain; the CH_2 stretching band at 2860 and 2930 cm^{-1}; the amide I, C=O band at 1630 cm^{-1}; the amid II, N-H vibration at 1535 cm^{-1}; and the C-H deformation band at 1460 and 1370 cm^{-1}. The associated peak at 730 cm^{-1} was due to the out-of-plane C-H bending.

Figure 4 shows optical images extracted from the camera recording at three particular load levels ε for loading of the as-received PLDA wire. The sample exhibited a typical tensile response of a synthetic polymer material, with a considerable stretching capability before breaking (Figure 4a). The examination of the tensile response showed a linear stage of up to 20% of the engineering strain, followed by a quasi-perfect plasticity stage and a notable elongation at break, allowing an elongation of 1.4 times its original length. A jagged behavior was also observed, which corresponded to irregularities or fluctuations in the stress–strain curve. These can be attributed to microstructural changes occurring unevenly or intermittently during loading. Table 3 summarizes the main engineering constants. In addition to a low stiffness that can be attributed to the low load rate and high sensitivity

of PLDA to strain rate, the yield stress (σ_Y) represents roughly 85% of the tensile strength (σ_M). There was no significant difference between the tensile strength and the ultimate stress ($\sigma_R \approx \sigma_M$). Furthermore, the elongation at break demonstrated significant variability, necessitating the use of a range of values to represent it rather than relying solely on the average and standard deviation.
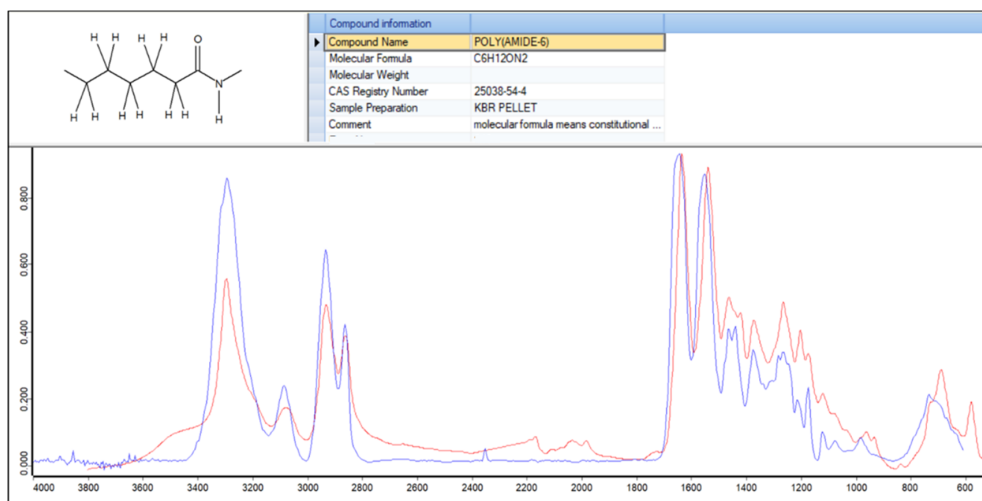

Figure 3. FTIR-ATR spectra of the studied filament, with typical polyamide taken as a reference: filament (red) and polyamide 6 (blue).

Table 3. Measured engineering constants for as-received and printed PLDA wires.

| Material	E_Y (MPa)	σ_Y (MPa)	σ_M (MPa)	σ_R (MPa)	ε_R (-)
PLDA wire	218 ± 33	36.7 ± 6.8	43.3 ± 4.2	42.8 ± 4.3	1.43–3.57
PLDA-T250-00-HOR	294 ± 15	46 ± 1.7	51 ± 2.5	45 ± 5.5	4.32 ± 0.52
PLDA-T260-00-HOR	255 ± 25	43 ± 3.2	45 ± 3.2	31 ± 6.4	2.55 ± 1.38
PLDA-T270-00-HOR	283 ± 26	47 ± 4.4	53 ± 2.5	47 ± 10.6	3.28 ± 2.08
PLDA-T280-00-HOR	291 ± 11	43 ± 1.8	48 ± 1.9	43 ± 1.9	4.51 ± 0.16
PLDA-T260-00-LAT	343 ± 13	50 ± 4.5	54 ± 6.5	52 ± 6.1	0.16 ± 0.02
PLDA-T260-00-VER	195 ± 66	21 ± 3.6	21 ± 3.6	21 ± 3.6	0.13 ± 0.05
PLDA-T260-15-HOR	277 ± 13	44 ± 2.1	46 ± 3.3	43 ± 1.4	4.35 ± 0.05
PLDA-T260-30-HOR	270 ± 31	45 ± 3.5	47 ± 3.4	43 ± 0.0	4.18 ± 0.00
PLDA-T260-45-HOR	272 ± 25	46 ± 3.5	48 ± 3.9	35 ± 2.3	3.45 ± 0.10

3.2. Tensile Behavior of 3D Printed PLDA

Figure 5 shows the equivalent tensile response of printed PLDA as a function of the printing temperature for a fixed orientation, corresponding to the horizontal printing configuration (i.e., building direction aligned with specimen thickness). Figure 5a shows the main stages of deformation for a typical specimen processed with a printing temperature of 250 °C and a layup of $-45°/+45°$. This layup allows a filament structuring in which both symmetrical in-plane and out-of-plane architectures are achieved. Indeed, material structuring is composed of a two-filament external frame, which wraps filament crossing at the exact angle of 45°. The external frame possesses a symmetrical structure in the longitudinal direction. Throughout the thickness of the specimen, two layers alternate with 45° and $-45°$ angles, allowing for a symmetrical configuration with respect to the central plane of the specimen. From each side of this plane, 13 symmetrical layers were printed. Homogeneous extension of the specimen was observed up to the first 30% of the increase in length, with a symmetrical behavior along the initial percentage of the material extension. A second stage corresponding to the necking formation at the center of the specimen followed, as shown at the engineering strain (ε) level of 0.79 (Figure 5a).

This stage corresponds to a first break in symmetry, as filaments in the central part were more subject to load transfer. Indeed, localization phenomena occurred when significant stretching of the filaments occurred. This localization corresponded to a reduction in the section of the filaments and thus to an asymmetrical behavior of the specimen. Due to the dog-bone geometry of the specimens, such localization was expected to be in the central part of the specimen. The necking achieved at large specimen extension locally modified the cross-section and propagated in the longitudinal direction to the grips. The expansion of such region towards the grip occurred ($\varepsilon = 2.51$) up to a point where failure was reached ($\varepsilon = 4.13$). This scenario was more or less the same for the other printing conditions, which was further examined through the tensile response in Figure 5b.
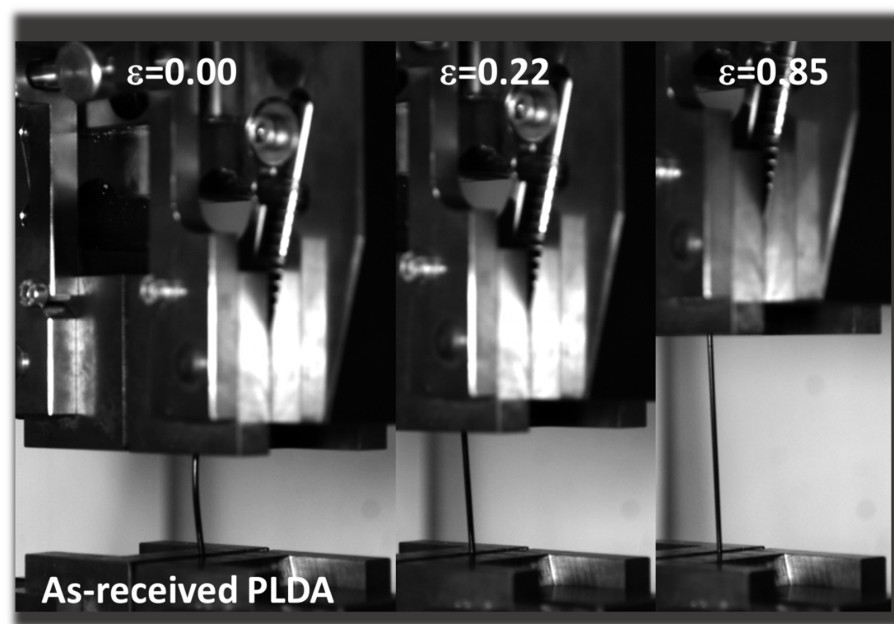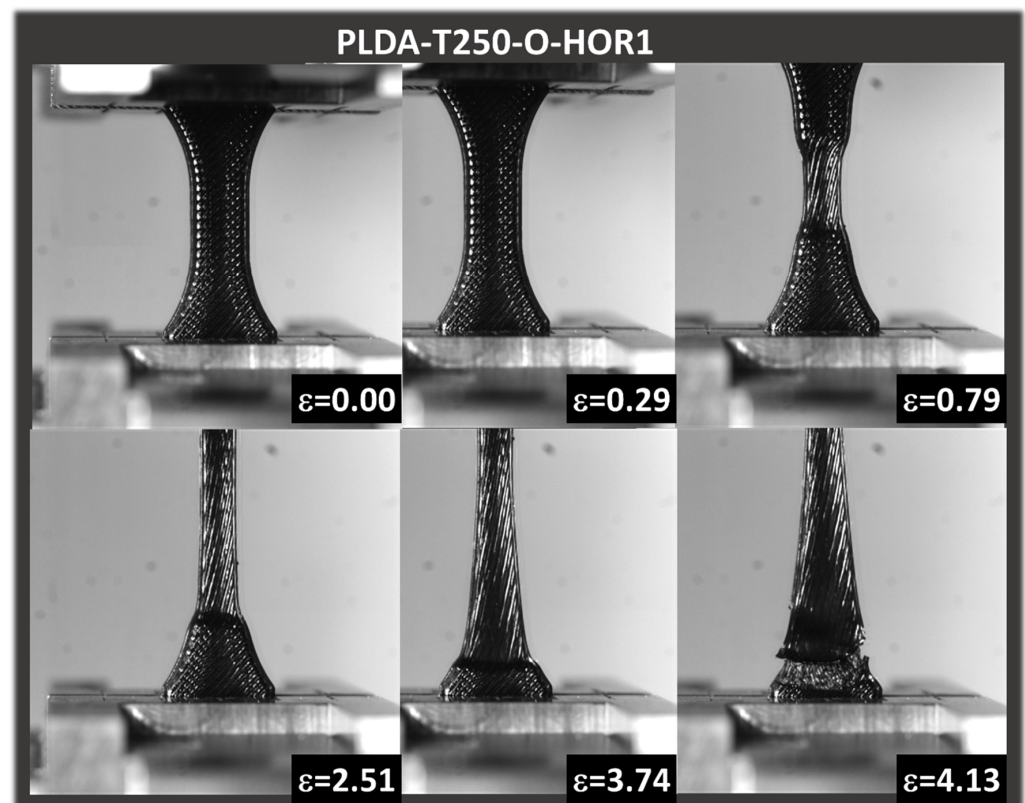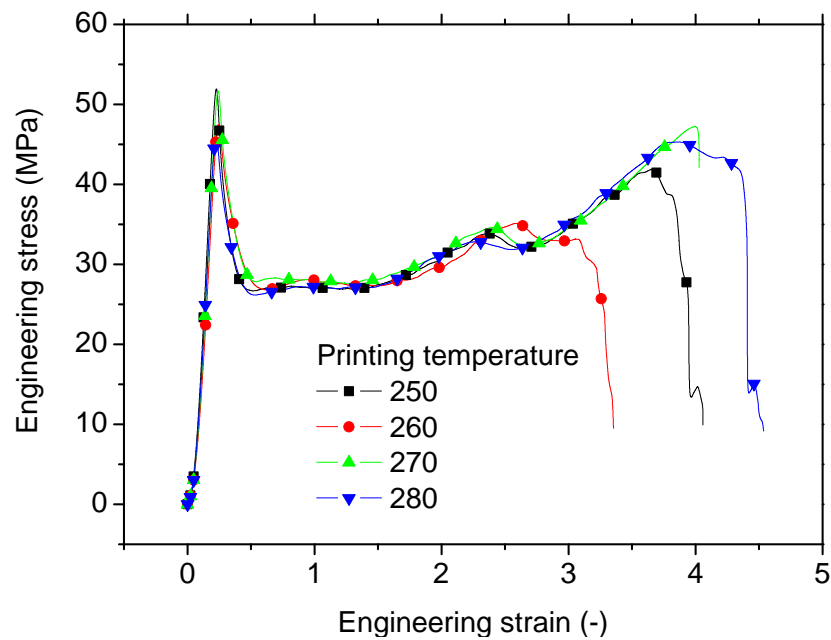

(**a**)
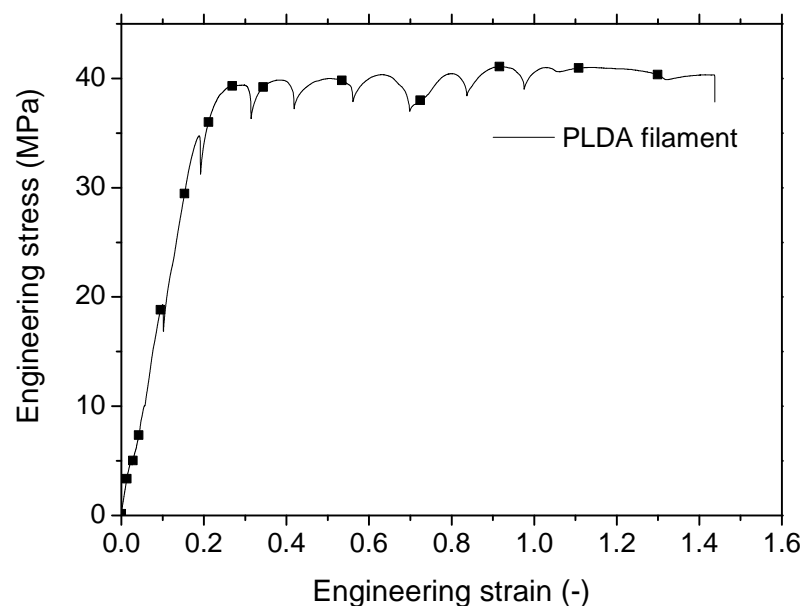
(**b**)

Figure 4. Tensile performance of as-received PLDA material. (**a**) Stretched PLDA at different loading levels, (**b**) engineering tensile response.

(**a**)

(**b**)

Figure 5. Tensile performance of 3D printed PLDA material as a function of the printing temperature for specimens printed in the horizontal direction (building direction//specimen thickness). (**a**) Deformed samples under various load levels, (**b**) engineering tensile response for a printing temperature between 250 °C and 280 °C.

No major differences were observed between the printing conditions within the printing temperature interval of 250–280 °C. The homogeneous extension refers here to the

first linear part of the tensile curve. A sudden drop in the stress from the tensile strength level occurred as a result of the necking, and a large plasticity stage followed. The rupture occurred after an increase in the stress, materialized by the alignment of the filaments in the loading direction and a stress localization. This stage partially restored the symmetry in the filament arrangement in the loading direction. This is referred to as a strain-stiffening behavior. There was no direct correlation between the stages mentioned above and the printing temperature. Table 3 further reenforces this statement. With the exception of the printing temperature 250 °C, there was a slight increase in Young's modulus by 15% and a large reduction in the elongation at break by 76%, depicted when the printing temperature increased from 260 °C to 280 °C. The increase in the stiffness of the material can be explained by the improvement in the coalescence phenomenon and the reduction in the necking effect that prevails between adjacent filaments [29]. The improvement in the stiffness comes at the expense of the reduction in the elongation at break.

The effect of printing temperature on the quality of the bond between adjacent filaments has been also observed for variety of materials. Pang et al. [30] reported this trend for PLA material processed between 180 °C and 240 °C. In addition, Hsueh et al. [31] studied the mechanical performance of 3D printed PLA and PETG. The authors also showed that the layer bond increased when the printing temperature increased. For most of the tests, a significant reduction in the elongation at break was correlated to improvements in the strength and stiffness.

No other tendencies for yield stress, tensile strength, and rupture stress were observed. Figure 6 shows the effects of the part orientation on the tensile performance of PLDA-printed samples for a fixed printing temperature of 260 °C. Deformed samples corresponding to vertical and lateral orientations are shown in Figure 6a. These can be fairly compared to the horizontal configuration shown in Figure 5a. A quasi-brittle failure was observed for both vertical and lateral orientations, with a limited stretching compared to the horizontal configuration. The homogeneous extension of the specimen up to the rupture point did not allow us to observe significant alterations in the material structuring. The entire loading can be fairly regarded as a process that preserves the symmetry up to the rupture point. However, at the rupture point, there was significant modification in the in-plane filament symmetry for the case of vertical orientation. This change in symmetry was triggered by crack initiation at the periphery of the specimen. The crack growth in the transverse direction was facilitated by the lack of cohesion between the filament arrangements in the longitudinal direction.

In the case of lateral orientation, a larger extension was depicted compared to the vertical one. The lateral orientation triggered a rupture in symmetry through the necking behavior, followed by a tendency to restore symmetry in the loading direction following filament realignment. The tensile responses of all the configurations are shown in Figure 6b, where all layups were fixed to −45°/+45° and the printing temperature was 260 °C. A clear distinction was found between the trend exhibited by the horizontal orientation (HOR) compared to the vertical (VER) and lateral (LAT) orientations. Even if higher stress levels were achieved in the lateral orientation, the same quasi-brittle behavior was observed for the VER and LAT orientations. The extracted engineering constants in Table 3 demonstrate the low ranking of VER for both Young's modulus and tensile strength compared to the remaining conditions.

In light of these results, it can be stated that the printing material did not exhibit isotropic behavior due to the sensitivity of the engineering quantities to the relative orientation of the loading direction with respect to the building direction. The measurement of anisotropic behavior can be estimated by taking the relative difference between the engineering constants for both the in-plane (LAT, HOR) and out-of-plane (VER) orientations.
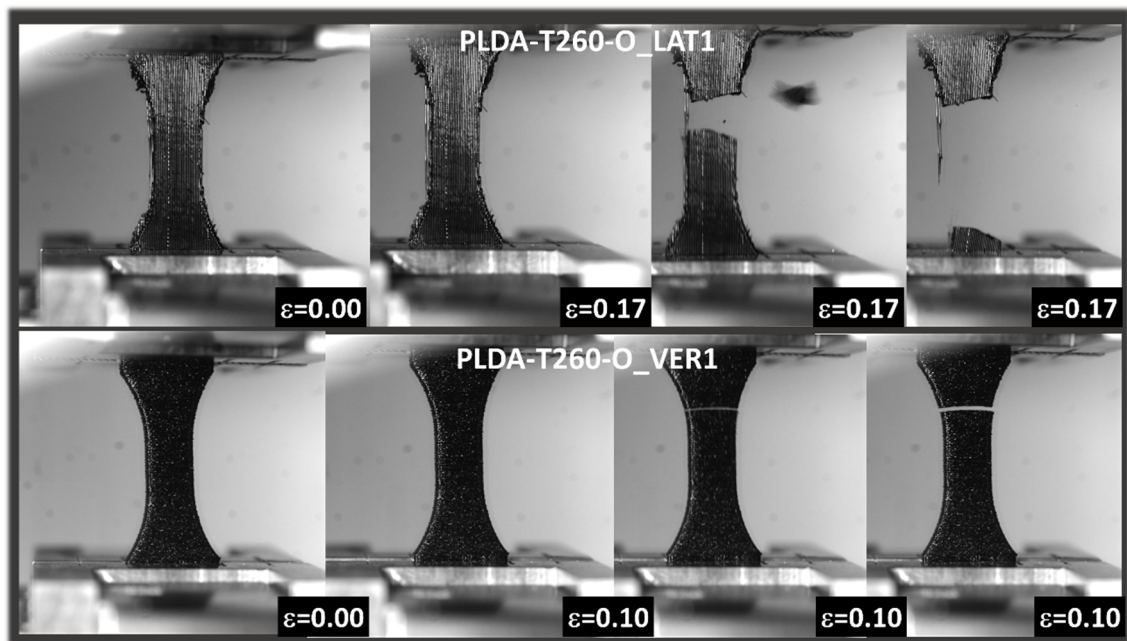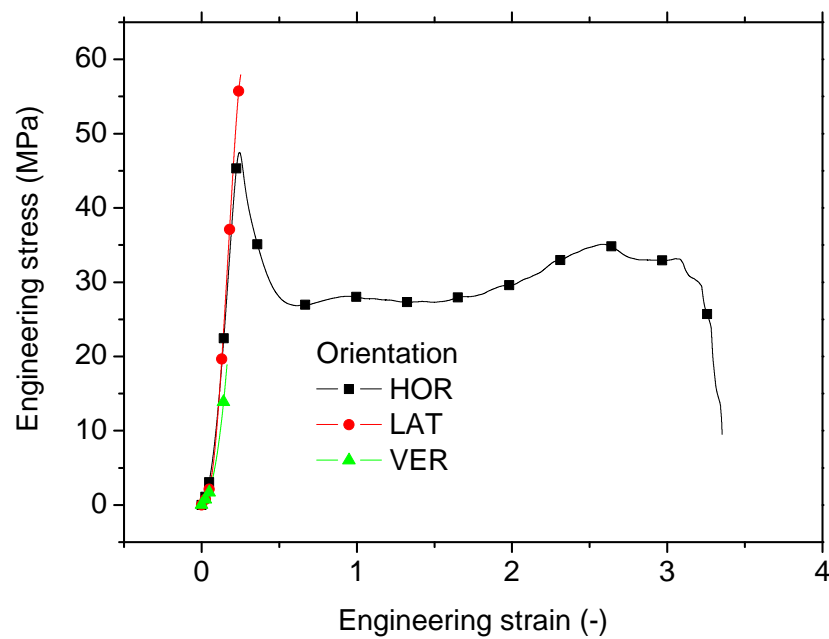
Figure 6. Effects of the part orientation on the tensile performance of 3D printed PLDA material for a fixed printing temperature of 260 °C. (**a**) Deformed samples for both vertical and lateral configurations under various load levels, (**b**) engineering tensile response of printed samples for all considered part orientations.

For the case of Young's modulus, this can be estimated using a printing angle of 0° as follows:

$$\alpha_E(-) = 1 - E_{VER}/AVE(E_{HOR},\ E_{LAT}) = 0.39 \tag{1}$$

where α_E is the anisotropy index and E refers to Young's modulus, and subscripts represent different studied orientations.

A similar index for tensile strength is as follows:

$$\alpha_E(-) = 1 - \sigma_{VER}/AVE(\sigma_{HOR}, \sigma_{LAT}) = 0.59 \tag{2}$$

where σ refers to the tensile strength.

An ideal isotropic behavior would provide a ground value for the anisotropy index.

At a consistent printing temperature of 260 °C, the stiffness of the specimens printed vertically is 76% in comparison to the horizontal orientation and 57% when compared to the lateral orientation. The lateral configuration is thus more suitable for improving the stiffness of the printed PLDA. The same observation also holds for the tensile strength, which is the highest for the lateral orientation. It ranks as 118% and 252% compared to the horizontal and vertical orientations, respectively. A severe reduction in the elongation at break was observed for the vertical and lateral orientations, which ranked only as 5% of the elongation at break for the horizontal orientation.

It can be concluded at this stage that the part orientation plays a major role in tuning the performance of 3D printed PLDA. This parameter influences the orientation of the filaments and their proportion in the loading direction. For the LAT configurations, a large amount of these filaments was oriented in the direction of loading, making it possible to maximize the load transfer through a uniaxial deformation. The HOR configuration partly exhibited this feature because the filaments composing the external frame were oriented in the loading direction and contributed to the load bearing capabilities of 3D printed PLDA. Also, the core filaments in this configuration were misaligned (depending on the printing angle) with respect to the loading direction and contributed more through a shear deformation. The VER configuration exhibited most of the filaments in the orthogonal direction and provided the lowest load-bearing capabilities.

Figure 7a shows the deformed samples corresponding to printing angles ranging from 0° to 45°.

Large filament stretching is a common feature for all printing angles prior to rupture. Such stretching is associated with a break in symmetry due to localized straining. In addition, filament realignment is the main driving mechanism, which allows the printed structure to withstand the tensile loading by modifying the symmetry of the filament in-plane arrangement. The intensity of the filament realignment depends on the printing angle. The filament realignment tends to restore material symmetry at later stages of loading. The intensity of the realignment is more significant for the configurations that exhibit the largest filament misorientation with respect to the loading direction. This was the case for the −45°/+45° angles.

Figure 7b depicts the tensile responses for all the studied printing angles. Even if the shape of the tensile response was the same for all the conditions, printing angles 15° and 30° exhibited the largest elongation at break due to the mechanism of filament alignment upon loading. This realignment was also responsible for improving the symmetry of the material, allowing a steady increase in the stress after the first stress peak. Regarding the quantified effects of the printing angle on the tensile performance (Table 3), there was no general trend other than an improvement in the stiffness when the specimens were printed using a printing angle larger than 0°. Although this improvement represented 7% of the total, the standard deviation obtained for Young's moduli data reflects a minor effect. Also, there was a slight increase in the tensile strength and yield stress of about 4%, as well as an increase in the elongation at break of 36%.
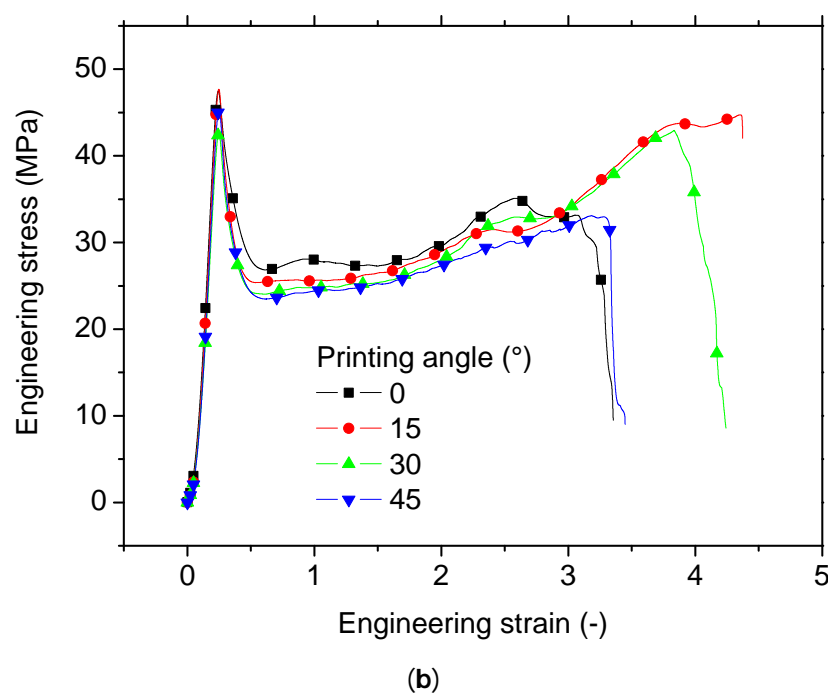
(**a**)

Figure 7. *Cont.*

(**b**)
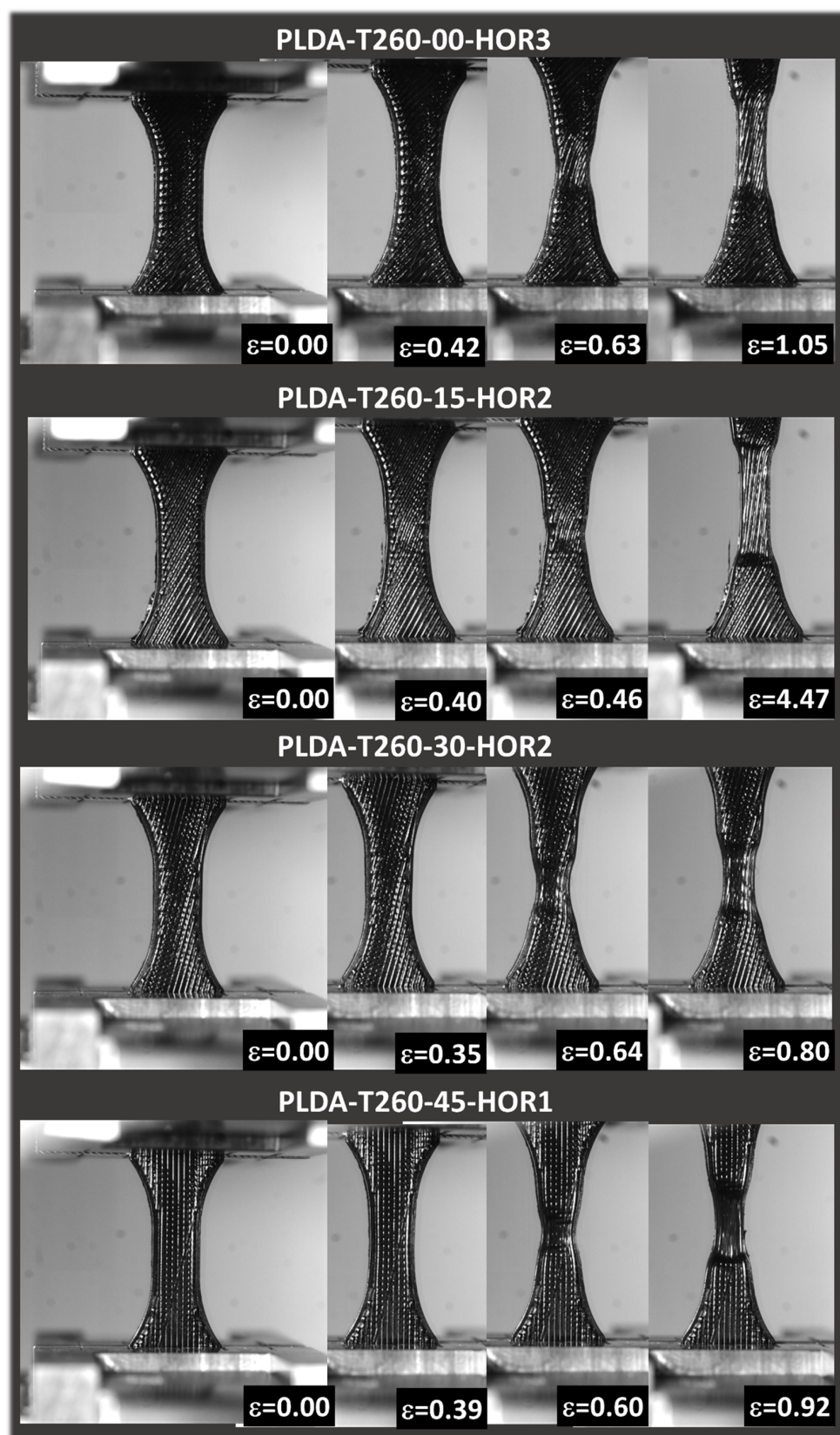
Figure 7. Effects of the printing angle on the tensile performance of 3D printed PLDA material for a fixed printing temperature of 260 °C. (**a**) Deformed samples for printing angles between 09° and 45°, (**b**) engineering tensile response of the printed samples for all the considered printing angles.

In order to provide further insight into the deformation mechanisms of 3D printed PLDA, imaging analysis is needed. At a low scale of approximately 1 μm, TEM (transmission electron microscopy) can provide information regarding fusion and structural mapping [32]. But, this method is more adequate for metallic-based materials obtained using AM, where a crystallographic arrangement at the atomic and nanometric scales can be significantly tuned through processing, such as processing of the columnal grain growth. In the case of polymeric materials, SEM analysis is more suitable, especially at the microstructural scale. This analysis was conducted for 3D printed PLDA, as shown in Figure 8. Among the identified modes of rupture, inter-filament decohesion was a common mode (micrograph on top left). It resulted from a lack of load transfer across the adjacent filaments. The large stretching of the filaments resulted in significant tearing of some filaments and the sudden breakage of others (micrographs on top right and bottom left). Depending on the loading and filament arrangements, mixed ruptures were observed more likely when transverse cracking of the filaments was combined with a large uniaxial extension (micrograph on bottom right).

Regarding the loss of the mechanical response when the PLDA was processed using the 3D printing route, Table 3 shows that the stiffness and elongation at break were on average increased by 26% and 109%, respectively. This increase was even larger if the vertical orientation was excluded from the pool (31%, 134%). The tensile strength was fully restored on average, with only a −1.5% lower value compared to the as-received wire material. It was even larger, with an up to 5% increase, when only the lateral and horizontal orientations were considered.
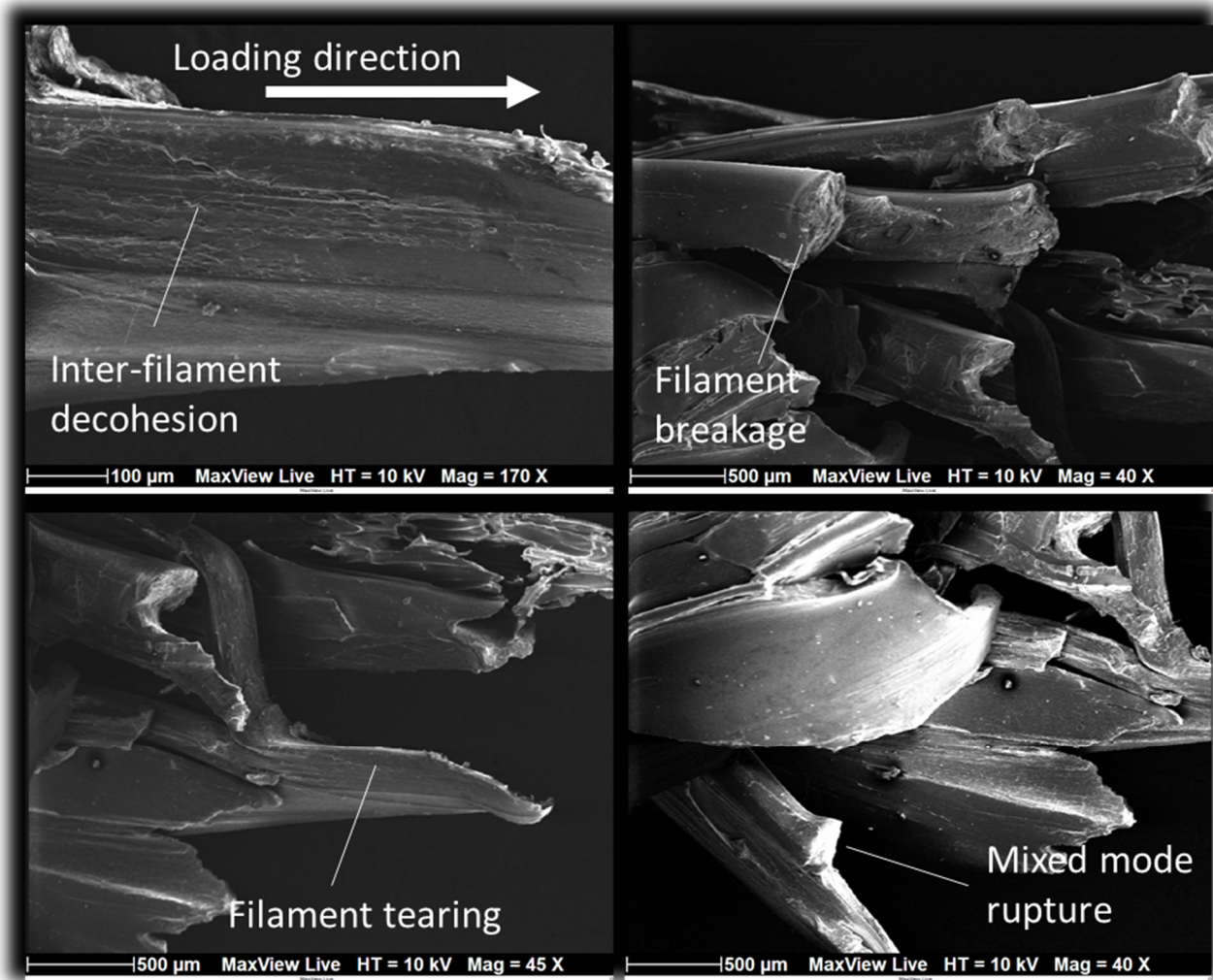
Figure 8. SEM micrographs showing the fractured surfaces and filament rupture modes of 3D printed PLDA (lateral views).

3.3. Microstructural Interpretation of Tensile Behavior

Figure 9 shows transverse and top views of the fractured surfaces. Filament realignment in the same direction of the external frame is highlighted by the micrograph on the top left. On the same micrograph, the large deformation of the filaments was responsible for the decohesion within the external frame, which was formed by two adjacent filaments. A transverse view of the fractured surface (micrograph on the top right) reveals the extent of the cracking along the longitudinal direction, which indicates the predominance of a mixed crack propagation mode combining the shear and crack opening. According to the same transverse view, the micrograph on the bottom left shows that the adjacent filament decohesion left a quasi-brittle fractured surface. Due to the way the filament was arranged throughout the thickness, these fragile surfaces became visible in every alternate pair of layers. Additionally, the significant tearing led to a deformation that occurred out of the plane, thereby contributing to the further propagation of the cracks in the longitudinal direction, as illustrated in the micrograph in the bottom right corner.
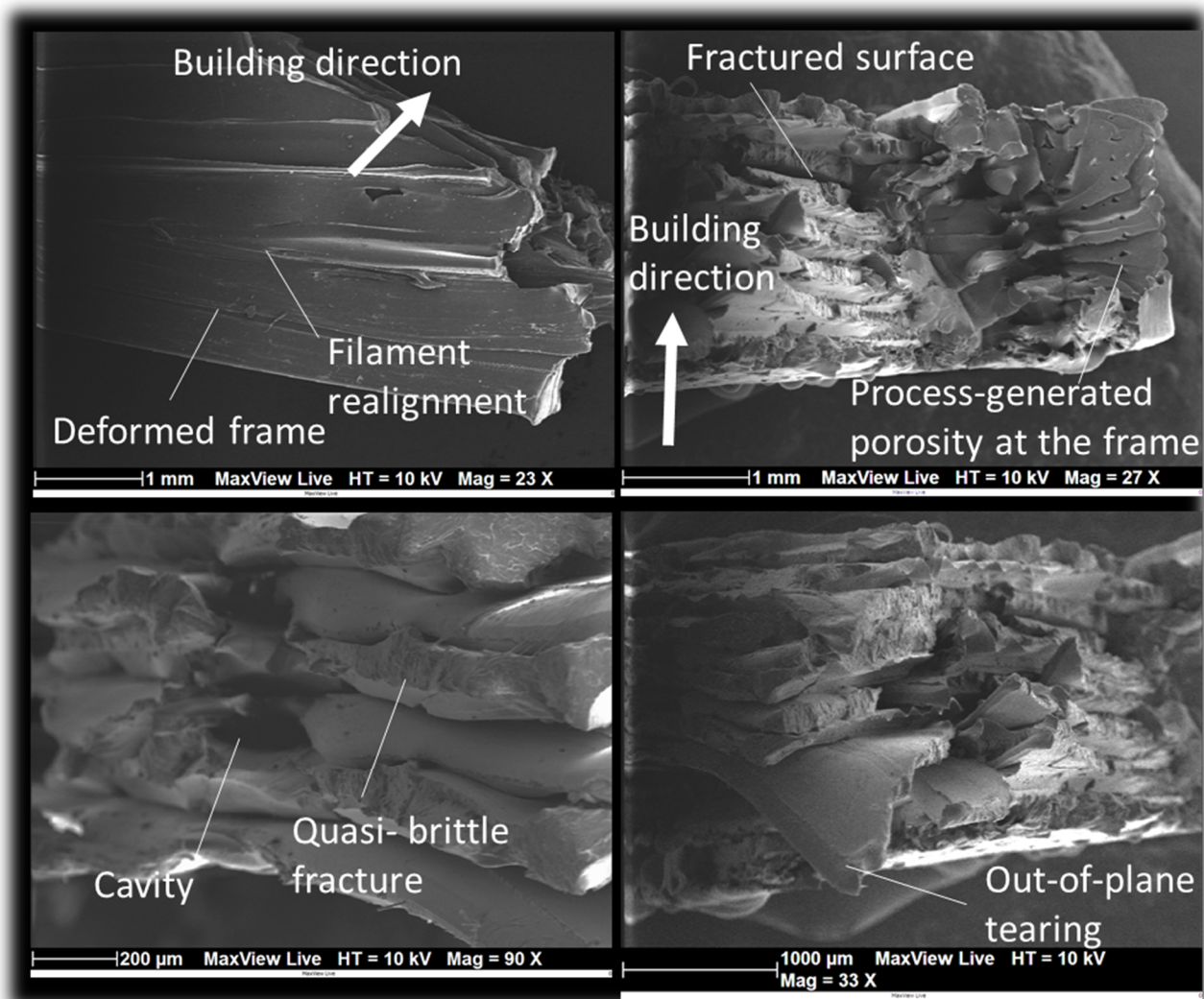
Figure 9. SEM micrographs showing the fractured surfaces and filament rupture modes in 3D printed PLDA (top and transverse views).

Figure 10 illustrates some of the localization phenomena observed upon rupture, which are related to the combination of large stretching and the filament arrangement. These localization phenomena reflect breaks in the material arrangement symmetry upon loading. On the top left, a rose-like pattern is highlighted where the filament tearing appears to cover all the possible in-plane angles. On the same micrograph, a strong contrast between the frame rupture is also illustrated, where on the arrowed side, a quasi-brittle rupture under tension opposes a more jagged cracking of the frame on the other side. Filament cross-section necking was also a common observation (see micrograph on the top right) in the plane perpendicular to the loading direction. Another feature is the longitudinal cracking responsible for the external frame unsoldering and the tored porosity (micrographs on the bottom).
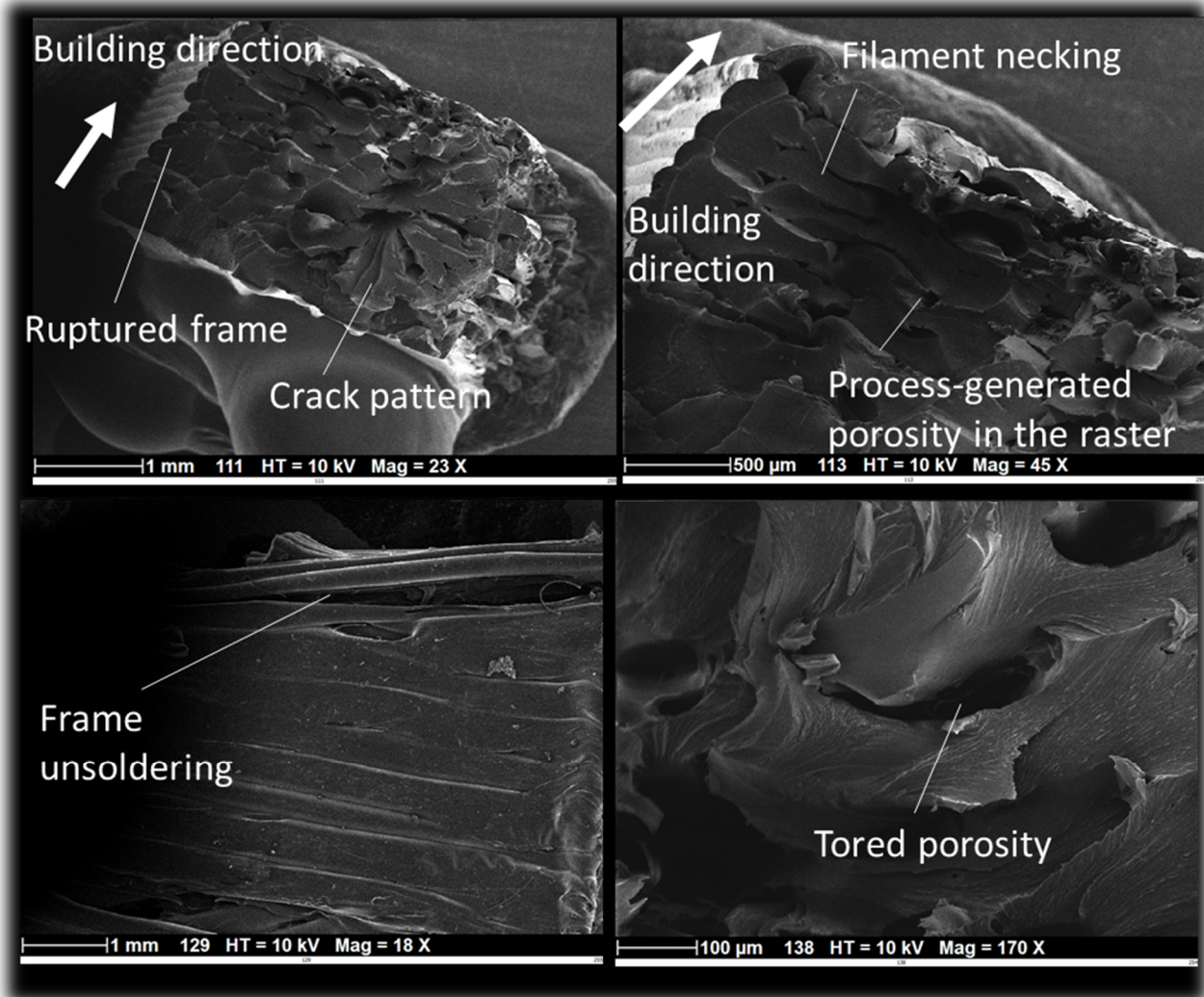
Figure 10. SEM micrographs showing localization phenomena and rupture modes in 3D printed PLDA.

3.4. Example of Application of PLDA in Bioengineering

In order to illustrate the use of PLDA in engineering applications, neck orthosis is considered as an application example. This structure, commonly referred to as a neck brace or cervical collar, is a medical device designed to provide support and stability to the neck and cervical spine. It is often used in the treatment of various neck injuries, such as whiplash, cervical fractures, or post-surgery recovery.

Figure 11a shows one particular style of neck orthosis called a rigid brace, which is used for more severe injuries. One of the main functions of this device is to help immobilize the neck, reducing movement and minimizing strain on injured or healing neck structures. The design is built by considering an airy structure to achieve a good compromise between material consumption and performance. Based on a structural analysis, finite element computation defines the strain field that matches realistic loading (Figure 11b). This analysis shows the development of a symmetrical stress field with two main regions of the stress concentration: close to the chin and chest support regions. This result reflects the stress field related to a transverse isotropic model with a longitudinal modulus (E_L = 291 MPa) that is aligned with the z-direction, which is 1.18 times lower than the two moduli in the X and Y directions (E_T = 343 MPa).
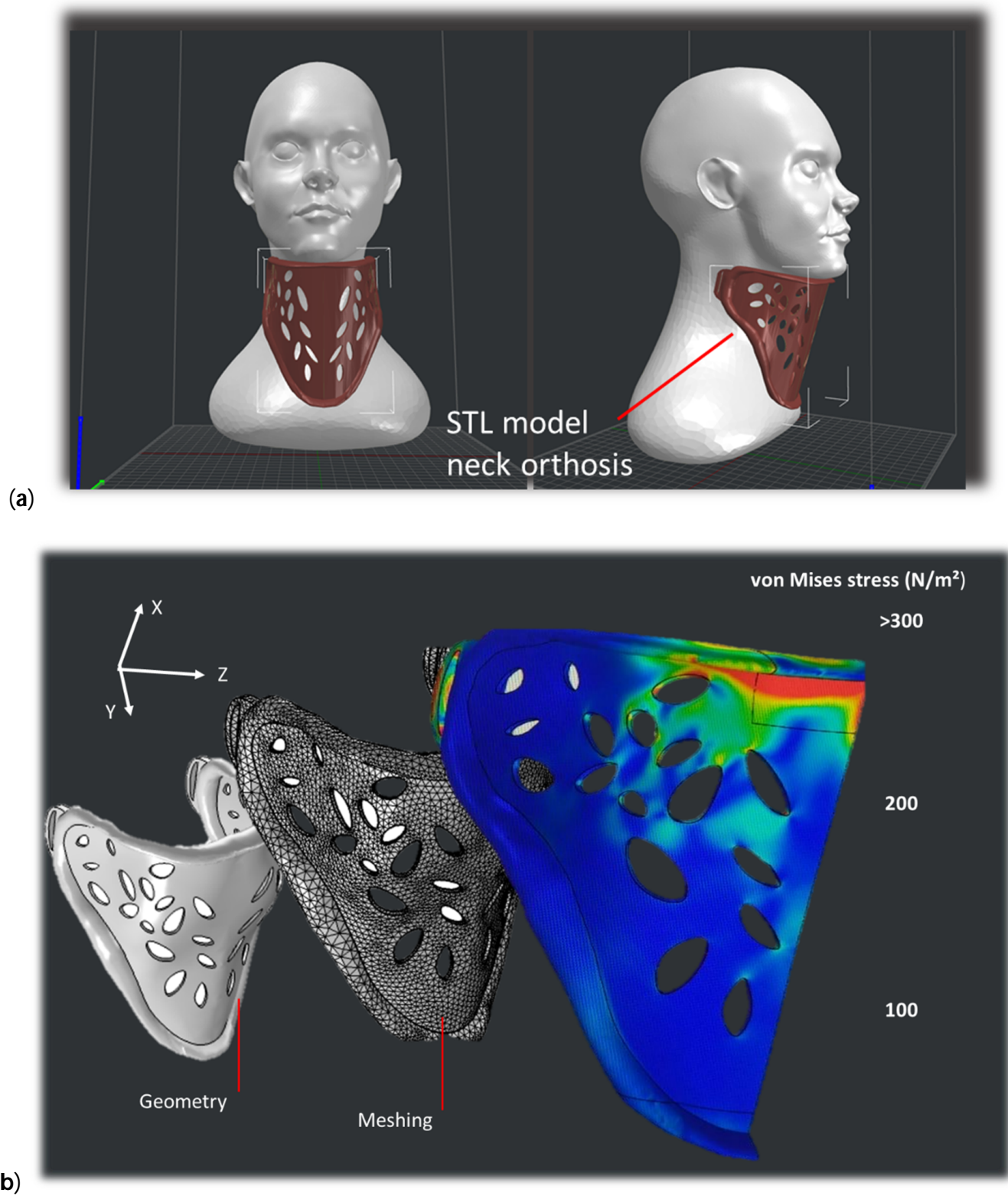
(a)

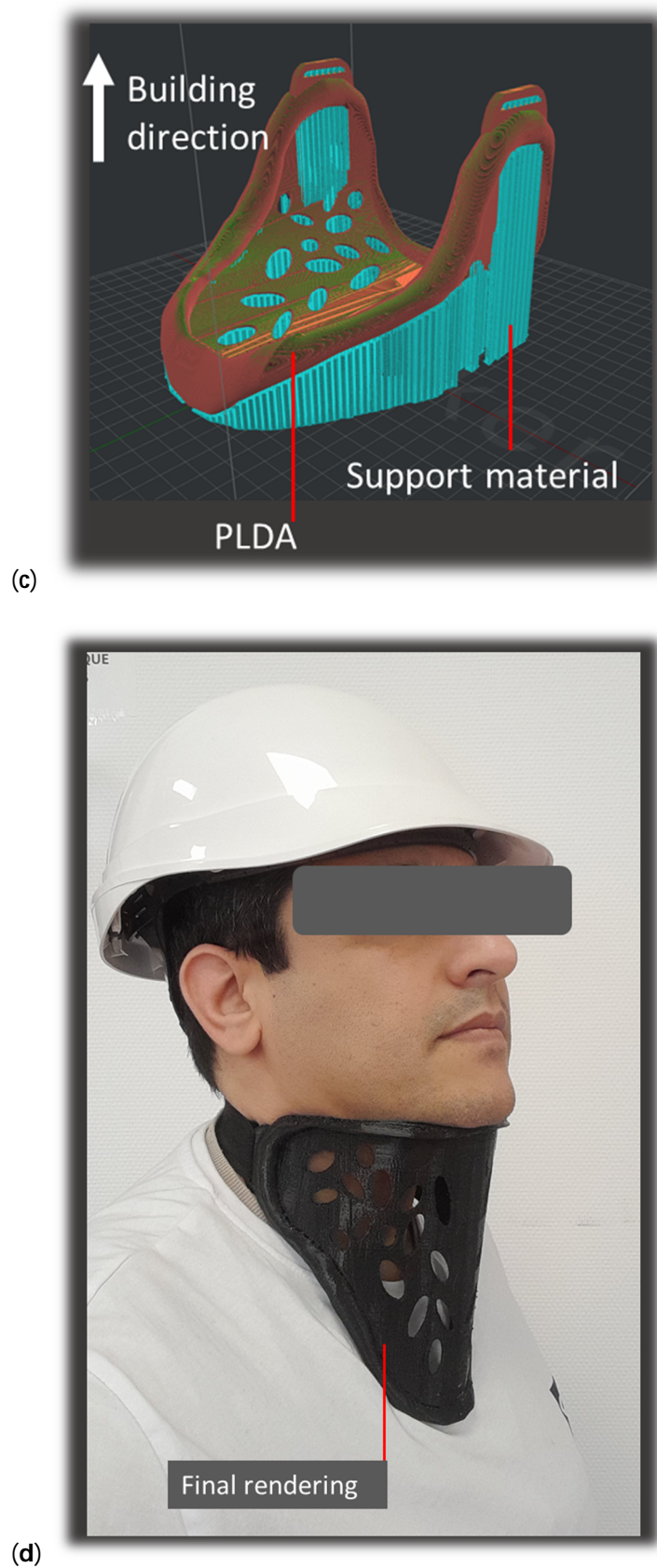(b)

Figure 11. *Cont*.

(**c**)

(**d**)

Figure 11. Design and manufacturing of neck orthosis: (**a**) CAD model of a rigid brace, (**b**) structural analysis showing the strain field in the device, (**c**) orientation of the part in the building platform, (**d**) final rendering of the printed prototype.

The design space corresponds to $142 \times 162 \times 117$ mm^3, and the optimized neck orthosis volume is 120 cm^3, for which 163 g of PLDA is required for the printing stage. The part orientation was selected to guarantee the continuity of the filaments along the areas subject to significant tension and to minimize the printing duration. The slicing step creates overhangs in the model, and the complexity of the neck orthosis design induces some risks of sagging or misshaping without support material. Thus, a support of the same material is added, as shown in Figure 11c, anywhere there is a risk of structure collapse. The amount of support represents 9% of the total design weight. The same printing conditions shown in Table 1 are used for printing the design, with the exception of the printing temperature, which is fixed to 260 °C. Under these conditions, a duration of 13.5 h is needed to print the design. Figure 11d shows the final rendering of the neck orthosis based on the PLDA material. It can be upgraded by using foam or fabric on top of the rigid brace structure to add more soft support for comfort.

4. Conclusions

One of the distinct features of PLDA is the remarkable increase in tensile properties when the material is processed using a fused filament route. Both the stiffness and elongation at break exhibited higher scores compared to the as-received material, with levels as large as 343 MPa, and 451% for Young's modulus and the elongation at break. The tensile strength was fully restored on average, with the largest level of 54 MPa.

The large stretchability of PLDA allows also for significant changes in the material arrangement symmetry, which affects the tensile response. For instance, strain stiffening is induced by change in the in-plane symmetry, which is materialized by the realignment of the filament in the loading direction. Within the printing temperature window of 250–280 °C, there was no significant influence observed other than a slight improvement in the stiffness by 15% and a reduction in elongation at break of 76% when the printing temperature was increased. The part orientation was found to play a major role in tuning the performance of the 3D printed PLDA, and it triggered significant changes in the symmetry in the filament arrangement. Both necking and filament realignment were associated with these symmetry modifications. The vertical orientation, in which the building direction is aligned with the sample length, was found to significantly reduce the stiffness by 76%. The lateral orientation, corresponding to filaments aligned in the loading direction, allowed for the highest tensile strength, with levels as large as 54 MPa. The printing angles of 15° and 30° were found to improve the elongation at break, taking advantage of the structural displacement induced by the filament realignment.

Regarding the deformation mechanisms, a combination of uniaxial tension and shearing was found to trigger different damage scenarios such as quasi-brittle and mixed-mode rupture, where transverse and longitudinal cracking predominated.

The remarkable performance of PLDA material allows it to be used in a variety of applications, such as in the biomedical field for ankle, foot, knee, wrist, and elbow orthoses. The successful design of a neck orthosis proves the effectiveness and the comfort of 3D printed PLDA, allowing for proper fitting and adjustment.

Data Availability Statement: The data that support the findings of this study are available from the corresponding author (SG), upon request.

References

1. Wu, Y.; Fang, J.; Wu, C.; Li, C.; Sun, G.; Li, Q. Additively manufactured materials and structures: A state-of-the-art review on their mechanical characteristics and energy absorption. *Int. J. Mech. Sci.* **2023**, *246*, 108102. [CrossRef]
2. *ISO/ASTM52900:2021*; Additive Manufacturing General Principles Fundamentals and Vocabulary. ISO: Geneva, Switzerland, 2021.
3. Yadav, A.; Rohru, P.; Babbar, A.; Kumar, R.; Ranjan, N.; Chohan, J.S.; Kumar, R.; Gupta, M. Fused filament fabrication: A state-of-the-art review of the technology, materials, properties and defects. *Int. J. Interact. Des. Manuf.* **2022**, *17*, 1–23. [CrossRef]
4. Rasiya, G.; Shukla, A.; Saran, K. Additive Manufacturing—A Review. *Mater. Today Proc.* **2021**, *47*, 6896–6901. [CrossRef]
5. Jadhav, A.; Jadhav, V.S. A review on 3D printing: An additive manufacturing technology. *Mater. Today Proc.* **2022**, *62*, 2094–2099. [CrossRef]
6. Shubham, P.; Sikidar, A.; Chand, T. The Influence of Layer Thickness on Mechanical Properties of the 3D Printed ABS Polymer by Fused Deposition Modeling. *Key Eng. Mater.* **2016**, *706*, 63–67. [CrossRef]
7. Bakır, A.A.; Atik, R.; Özerinç, S. Mechanical properties of thermoplastic parts produced by fused deposition modeling: A review. *Rapid Prototyp. J.* **2021**, *27*, 537–561. [CrossRef]
8. Lee, C.-Y.; Liu, C.-Y. The influence of forced-air cooling on a 3D printed PLA part manufactured by fused filament fabrication. *Addit. Manuf.* **2019**, *25*, 196–203. [CrossRef]
9. Khatoon, S.; Ahmad, G. Rapid prototyping of 3d printed micropillars using fused filament fabrication technique for biomedical applications. *Rapid Prototyp. J.* **2023**, *29*, 2272–2284. [CrossRef]
10. Jin, Y.-A.; Plott, J.; Chen, R.; Wensman, J.; Shih, A. Additive Manufacturing of Custom Orthoses and Prostheses—A Review. *Procedia CIRP* **2015**, *36*, 199–204. [CrossRef]
11. Carrico, J.D.; Traeden, N.W.; Aureli, M.; Leang, K.K. Fused filament 3D printing of ionic polymer-metal composites (IPMCs). *Smart Mater. Struct.* **2015**, *24*, 125021. [CrossRef]
12. Feng, J.; Fu, J.; Lin, Z.; Shang, C.; Li, B. A review of the design methods of complex topology structures for 3D printing. *Vis. Comput. Ind. Biomed. Art* **2018**, *1*, 5. [CrossRef]
13. Abouzaid, K.; Guessasma, S.; Belhabib, S.; Bassir, D.; Chouaf, A. Printability of co-polyester using fused deposition modelling and related mechanical performance. *Eur. Polym. J.* **2018**, *108*, 262–273. [CrossRef]
14. Lin, X.; Gao, J.; Wang, J.; Wang, R.; Gong, M.; Zhang, L.; Lu, Y.; Wang, D.; Zhang, L. Desktop printing of 3D thermoplastic polyurethane parts with enhanced mechanical performance using filaments with varying stiffness. *Addit. Manuf.* **2021**, *47*, 102267. [CrossRef]
15. Guessasma, S.; Belhabib, S.; Nouri, H. Microstructure, Thermal and Mechanical Behavior of 3D Printed Acrylonitrile Styrene Acrylate. *Macromol. Mater. Eng.* **2019**, *304*, 1800793. [CrossRef]
16. Dana, H.R.; El Mansori, M. Investigations on the mechanical properties of PLA/Flax fibre composites obtained by Fused Filament Fabrication. *Plast. Rubber Compos.* **2022**, *51*, 393–406. [CrossRef]
17. Doğru, A.; Sözen, A.; Seydibeyoğlu, M.Ö.; Neşer, G. Hemp Reinforced Polylactic Acid (PLA) Composite Produced by Fused Filament Fabrication (FFF). *Hacet. J. Biol. Chem.* **2022**, *50*, 239–246. [CrossRef]
18. Kananathan, J.; Samykano, M.; Kadirgama, K.; Ramasamy, D.; Rahman, M.M. Comprehensive investigation and prediction model for mechanical properties of coconut wood–polylactic acid composites filaments for FDM 3D printing. *Eur. J. Wood Wood Prod.* **2021**, *80*, 75–100. [CrossRef]
19. Chaunier, L.; Guessasma, S.; Belhabib, S.; Della Valle, G.; Lourdin, D.; Leroy, E. Material extrusion of plant biopolymers: Opportunities & challenges for 3D printing. *Addit. Manuf.* **2018**, *21*, 220–233. [CrossRef]
20. Guessasma, S.; Belhabib, S.; Altin, A. On the Tensile Behaviour of Bio-Sourced 3D-Printed Structures from a Microstructural Perspective. *Polymers* **2020**, *12*, 1060. [CrossRef]
21. Uralde, V.; Veiga, F.; Aldalur, E.; Suarez, A.; Ballesteros, T. Symmetry and Its Application in Metal Additive Manufacturing (MAM). *Symmetry* **2022**, *14*, 1810. [CrossRef]
22. Jagadeesh, B.; Duraiselvam, M.; Prashanth, K.G. Deformation behavior of metallic lattice structures with symmetrical gradients of porosity manufactured by metal additive manufacturing. *Vacuum* **2023**, *211*, 111955. [CrossRef]
23. Ahn, S.-H.; Montero, M.; Odell, D.; Roundy, S.; Wright, P.K. Anisotropic material properties of fused deposition modeling ABS. *Rapid Prototyp. J.* **2002**, *8*, 248–257. [CrossRef]
24. Hedjazi, L.; Belhabib, S.; D'Orlando, A.; Guessasma, S. Breaking Material Symmetry to Control Mechanical Performance in 3D Printed Objects. *Symmetry* **2022**, *15*, 28. [CrossRef]
25. Fayazbakhsh, K.; Movahedi, M.; Kalman, J. The impact of defects on tensile properties of 3D printed parts manufactured by fused filament fabrication. *Mater. Today Commun.* **2019**, *18*, 140–148. [CrossRef]
26. Zhang, X.; Fan, W.; Liu, T. Fused deposition modeling 3D printing of polyamide-based composites and its applications. *Compos. Commun.* **2020**, *21*, 100413. [CrossRef]

27. Arigbabowo, O.K.; Omer, L.; Tate, J. Fused filament fabrication of polyamide 6 nanographene composite for electrostatic discharge applications. *Mater. Sci. Eng. B* **2023**, *287*, 116086. [CrossRef]

28. Belei, C.; Joeressen, J.; Amancio-Filho, S.T. Fused-Filament Fabrication of Short Carbon Fiber-Reinforced Polyamide: Parameter Optimization for Improved Performance under Uniaxial Tensile Loading. *Polymers* **2022**, *14*, 1292. [CrossRef]

29. Thadasack, M.; Réguerre, A.-L.; Leroy, E.; Guessasma, S.; Lourdin, D.; Weitkamp, T.; Chaunier, L. Tuning pharmaceutically active zein-based formulations for additive manufacturing. *Addit. Manuf.* **2023**, *78*, 103849. [CrossRef]

30. Pang, R.; Lai, M.K.; Ismail, K.I.; Yap, T.C. The Effect of Printing Temperature on Bonding Quality and Tensile Properties of Fused Deposition Modelling 3D-Printed Parts. *IOP Conf. Ser. Mater. Sci. Eng.* **2022**, *1257*, 012031. [CrossRef]

31. Hsueh, M.-H.; Lai, C.-J.; Wang, S.-H.; Zeng, Y.-S.; Hsieh, C.-H.; Pan, C.-Y.; Huang, W.-C. Effect of Printing Parameters on the Thermal and Mechanical Properties of 3D-Printed PLA and PETG, Using Fused Deposition Modeling. *Polymers* **2021**, *13*, 1758. [CrossRef]

32. Zhu, W.; Hangas, J.; Li, Y.; Huo, Y.; Poczatek, E.; Li, M. TEM Study on the Additive-Manufactured AlSi10Mg. *Microsc. Microanal.* **2020**, *26*, 3228–3231. [CrossRef]